Check for updates

Coordination environment and architecture engineering over Co$_4$N-based nanocomposite for accelerating advanced oxidation processes

Ping Li [a,b,*], Yunan Lin [a,b], Quhua Huang [a,b], Wenqin Li [a,b], Shien Zhao [a,b], Yi Fu [a,b], Feng Chu [a,b], Shuanghong Tian [a,b,*]

[a] School of Environmental Science and Engineering, Sun Yat-sen University, Guangzhou 510275, Guangdong, PR China
[b] Guangdong Provincial Key Laboratory of Environmental Pollution Control and Remediation Technology, Guangzhou 510275, PR China

ABSTRACT

Innovating new Co-based materials to outperform widely-used Co$_3$O$_4$-based ones for eliminating recalcitrant pollutants via peroxymonosulfate (PMS) activation is dauntingly challenging. Herein we highlight for the first time that Co$_4$N is a new-generation PMS activator, and illuminate comprehensive understanding of intrinsic activity correlated with coordination environment of Co site. The nanocomposite comprising Co$_4$N nanoparticles immobilized on rGO, derived from a metal-organic complex, presents remarkable catalysis for 4-chlorophenol degradation via PMS activation, particularly, up to 42 times of promotion is harvested relative to Co$_3$O$_4$-based catalyst with similar morphology (0.682 vs 0.016 min^{-1}). Theoretical calculations unravel that with respect to the common-used Co$_3$O$_4$ and Co, Co$_4$N featuring N incorporated into interstices of Co framework has more suitable electronic structure to render optimal binding strength for PMS activation. This work points to the potential of Co-based nitrides for PMS activation, and enlightens that subtle engineering over coordination environment and architecture promises boosted catalysis.

1. Introduction

The ever-increasing water pollution and fresh water scarcity have aroused huge concern over the decades. Advanced oxidation processes (AOPs) have been demonstrated to be a class of powerful techniques to degrade recalcitrant organic pollutants through taking advantage of reactive oxygen species (ROS) [1–6]. Among various AOPs, sulfate radical (SO$_4^{\bullet-}$)-based advanced oxidation processes (SR-AOPs) through the activation of peroxymonosulfate (PMS) have received a great deal of research attention for water purification, since SO$_4^{\bullet-}$ species possesses stronger oxidizing capability, wider pH range adaptability and longer lifetime with respect to •OH species, which is the main ROS in classical Fenton system using hydrogen peroxide (H$_2$O$_2$) [7–11].

In general, SO$_4^{\bullet-}$ can be readily generated from PMS by using various transition metal-based activators, and Co-based catalysts has been proved to be the most efficient PMS activator [12,13]. Considering the secondary pollution and catalyst recovery difficulty accompanied by the homogeneous Co^{2+} system, exploring heterogeneous Co-based catalysts is undoubtedly more preferable [8,14,15]. At the current stage, the overwhelming majority of researches on heterogeneous Co-based

catalysts focus on Co-containing metals and oxides [16–19], whereas their catalytic properties in SR-AOPs are still not satisfactory, seriously impeding advancing their practical applications. In this regard, exploring and innovating new Co-based materials, which can enrich the catalyst family for PMS activation, presents a promising route to make breakthroughs on further promoting catalytic performance.

On another front, in the past decade, transition metal nitrides (TMN) have attracted a tremendous amount of attention in various renewable energy systems (e.g., fuel cells, rechargeable batteries, water electrolyzer, etc.), owing to their unique physicochemical characteristics including good stability, excellent conductivity and metallic property [20–26]. Nevertheless, so far, utilizing TMN as the PMS activator for organic pollutant elimination is rarely reported. In general, for the transition metal compound catalysts, the transition metal species functions as the active site, and its intrinsic catalytic activity can be effectively modulated by the surrounding anionic structure via electronic state tuning [27–29]. Based on the above analysis, it is understandable that the TMN with nonmetal N coordination can exhibit distinct catalytic properties in comparison with the zero-valent metallic TM as well as TM oxides. Plus, considering the aforementioned merits of TMN, it

could be reasonable to expect that TMN hold large potent for boosted SR-AOPs. The pioneering work by Wang et al. discovered that FeCo alloy coupled with Mn_4N can display recommendable catalytic performance to degrade bisphenol A through PMS activation, to some extent, suggesting the feasibility of TMN for accelerating SR-AOPs [30]. Despite the progress made, exploiting and innovating high-performing TMN for PMS activation is strongly desired, yet challenging. Equally importantly, a comprehensive understanding of the effect of N species on the electronic structure and local coordination environment of the metal sites, and further on the intrinsic catalytic activity of TMN for PMS activation is still lacking, detailed interpretation is imperatively required for guiding TMN to advance AOPs.

Motivated by the above considerations, in this contribution, we present, for the first time, the engineering of 2D reduced graphene oxide nanosheet supported Co_4N nanocomposite (rGO/Co_4N) for promoting PMS activation to degrade recalcitrant organics. The rGO/Co_4N nanocomposite is constructed via a facile and controllable metal-organic complex (MOC)-mediated approach. The selection of the rGO nanosheet as substrate herein could immobilize fine Co_4N nanoparticles (NPs) with high dispersion and strong robustness, contributing to exposing catalytic sites and accelerating mass transfer for catalysis. Meanwhile, rGO incorporation could further accelerate charge transfer for AOPs. Encouragingly, the catalytic property investigation demonstrates that rGO/Co_4N nanocomposite can exhibit outstanding catalytic performance for oxidative degradation of the organic pollutants via activation of PMS, much superior to the corresponding supported Co_3O_4 and Co counterparts. Based on the systematical theoretical calculations, it is disclosed that relative to the widely-studied Co_3O_4 and metallic Co, Co_4N with N incorporated into the interstices of the Co framework could possess more desirable electronic structure and coordination environment, favorably leading to optimized binding strength for PMS activation.

2. Experimental section

2.1. Preparation of the rGO/Co₄N nanocomposite

The graphene oxide (GO) was synthesized through the Hummer's route with some modifications [31]. The precursor rGO/Co-MOC was synthesized in the following steps. Initially, 1 mmol of Co $(CH_3COO)_2 \cdot 4H_2O$, 3 mmol of urea, 2.5 mg of GO, and 0.322 g of polyvinylpyrrolidone (PVP) were added in 20 mL of ethylene glycol (EG) and then ultra-sonicated. Afterwards, the as-obtained homogeneous suspension was heated at 182 ℃ for 3 h with an oil bath. The as-obtained gray precipitate product was centrifuged, rinsed, and dried at 60 °C. As for the fabrication of the rGO/Co_4N nanocomposite, 30 mg of the rGO/Co-MOC precursor (at the downstream) and a certain amount of urea (at the upstream) were placed in a porcelain boat, and then charged in a quartz tube and heated at 450 ℃ (ramping rate: 2 ℃/min) for 2 h under a N_2 flowing.

2.2. Preparation of a series of the controls

rGO: The rGO sample was prepared via adopting the same route for $rGO/Co-MOC$ while without the addition of $Co(CH_3COO)_2 \cdot 4H_2O$.

Free-standing Co_4N: The Co_4N sample was synthesized via adopting the same route for rGO/Co_4N while GO was not added.

rGO/Co_3O_4: The rGO/Co_3O_4 sample was prepared by directly calcinating the rGO/Co-MOC precursor in a muffle furnace at 300 ℃ (ramping rate: 2 ℃/min) for 2 h.

rGO/Co: The rGO/Co sample was prepared by thermal reduction of the rGO/Co-MOC precursor at 450 ℃ (ramping rate: 2 ℃/min) for 2 h under a H_2 flowing.

2.3. Catalytic performance investigation

To evaluate catalytic performance of the samples, the degradation of the model contaminant 4-chlorophenol (4-CP) was conducted (reaction temperature = 20 ℃). In a typical reaction, the solid catalyst powder (2 mg) was added in 40 mL of 4-CP aqueous solution (50 mg/L). After the above suspension was shaken for a period time of 30 min with assistance of a continuous shaking bath, oxone (20 mg, as the PMS source) was added to start the catalytic reaction. To monitor the reaction process, at selected time intervals, 1 mL of the reaction mixture was collected, quenched with ethanol, and filtered for further analysis. To perform the reusability investigation, the used rGO/Co_4N was filtered, washed, dried, and then reused in the following runs, in which the same reaction conditions were used.

The quenching experiment was performed using the same reaction conditions while feeding additional scavenging agent, such as sodium azide (NaN_3), methanol (MeOH), tert-butyl alcohol (TBA), and p-benzoquinone (p-BQ).

In electron paramagnetic resonance (EPR) study, the spin-trapping agents, including 2,2,6,6-tetramethyl-4-piperidine (TEMP) and 5,5-dimethyl-1-pyrroline-N-oxide (DMPO) were utilized.

The impact of reaction temperature on catalytic 4-CP removal was investigated with similar testing condition while the initial concentration of 4-CP was adjusted to 60 mg/L for better observation and analysis. Herein the reaction temperatures of 20, 30, and 40 ℃ were selected for evaluation.

The catalytic oxidative removal of other model contaminants, such as ibuprofen (IBP, 20 mg/L), bisphenol A (BPA, 25 mg/L), and florfenicol (FF, 20 mg/L), were carried out with the same testing conditions for those of 4-CP.

The concentrations of the organic contaminants studied in this work were analyzed using the liquid chromatography system (LC-16, SHIMADZU, C18 column + UV detector).

3. Results and discussion

3.1. Preparation and structural characterization

The preparation of rGO/Co_4N nanocomposite involves two steps as illustrated in Scheme 1. First, rGO/Co-MOC precursor was fabricated via the coordination reaction between Co^{2+} and EG in the presence of GO suspension at elevated temperature. Second, such as-obtained rGO/Co-MOC was subjected to a pyrolysis treatment together with urea under N_2 atmosphere. During this process, urea was thermally decomposed to release NH_3, which can serve as nitrogen source to convert rGO/Co-MOC to rGO/Co_4N via a nitridation reaction. Here it is worth mentioning that with respect to the conventional NH_3 gas, which is flammable and corrosive, undoubtedly, urea is a greener and safer nitrogen source for nitridation treatment.

The SEM and TEM techniques were firstly performed to investigate morphological structures of samples. As presented in Fig. 1a–c, the rGO/Co-MOC precursor holds 2D nanosheet morphology with a relatively rougher and thicker surface in comparison with the pristine ultrathin and smooth GO nanosheets. In the XRD pattern of rGO/Co-MOC shown in Fig. 2a, the emergence of the diffraction peak at around 10° can be assigned to the typical characteristics for the layered metal alkoxide complexes, demonstrating the formation of metal alkoxide species, that is, Co-MOC in the precursor [32,33]. Further, from the FTIR spectrum in Fig. 2b, the peaks at 2850–2960 cm^{-1} and 130–1460 cm^{-1} can be assigned to C–H stretching and bending vibrations, respectively; the peak at 1060–1130 cm^{-1} is for C–O stretching vibration; and the peak at 510–604 cm^{-1} is for Co-O stretching vibration, collectively signify the successful complexation between Co species and EG ligand in the rGO/Co-MOC precursor [33–35].

By a subsequent gas–solid nitridation treatment with the assistance of urea, the rGO/Co-MOC precursor was converted to rGO/Co_4N
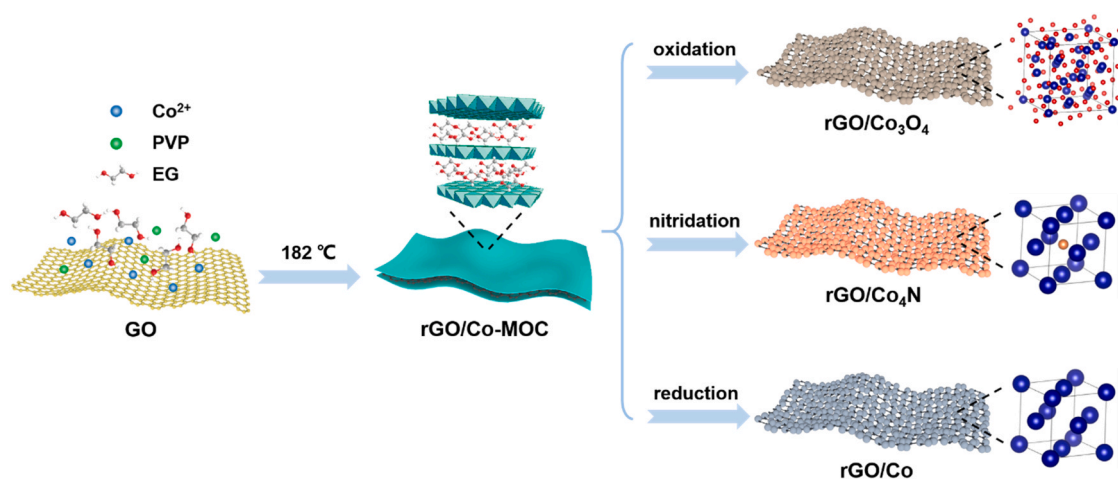
Scheme 1. The schematic illustration for the synthetic procedures of the rGO/Co$_4$N, rGO/Co$_3$O$_4$, and rGO/Co nanocomposites.
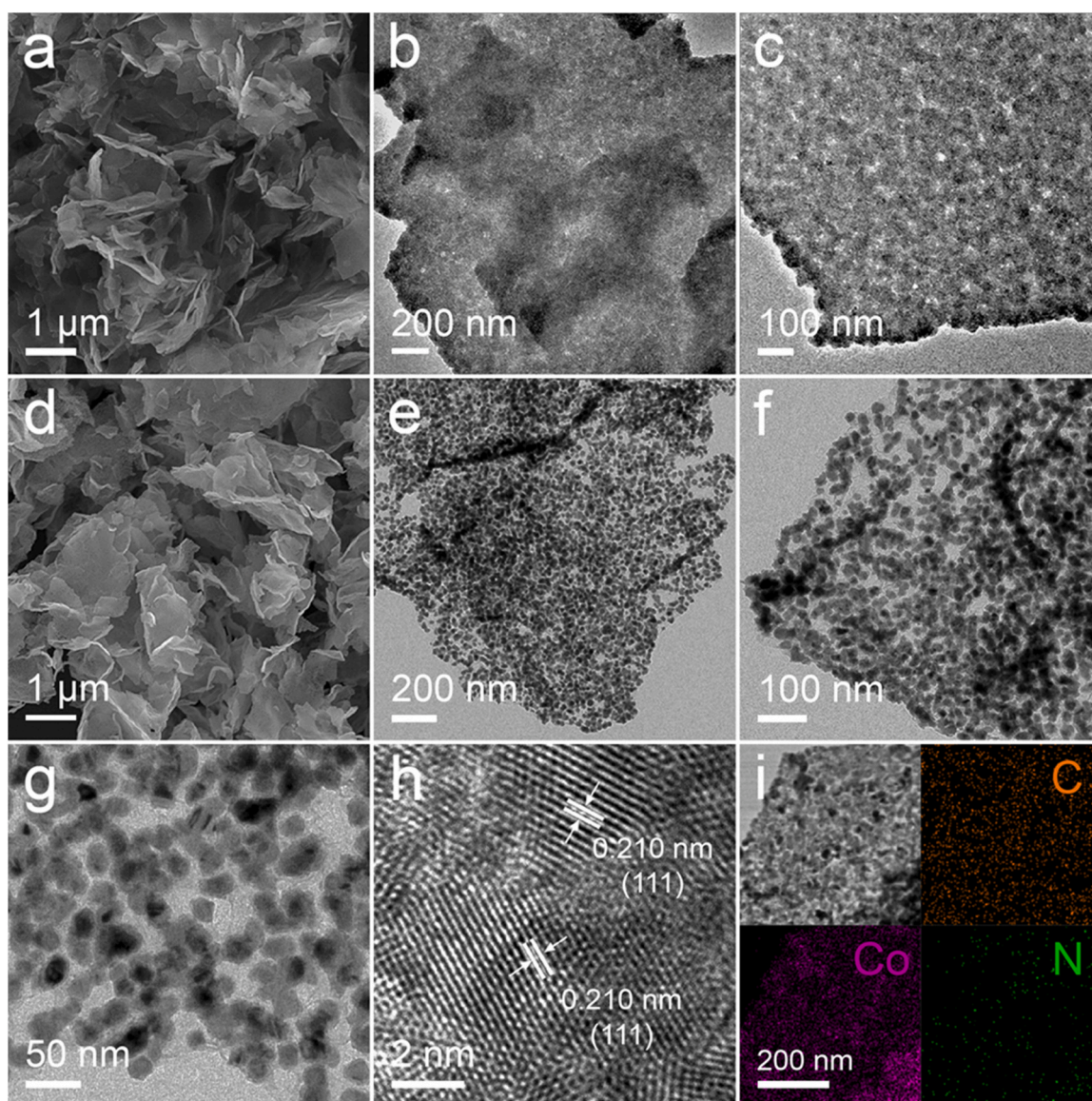

Fig. 1. (a) SEM image and (b,c) TEM images of the rGO/Co-MOC precursor. (d) SEM image, (e-g) TEM images, (h) HRTEM image, and (i) EDX elemental mappings of the rGO/Co$_4$N nanocomposite.
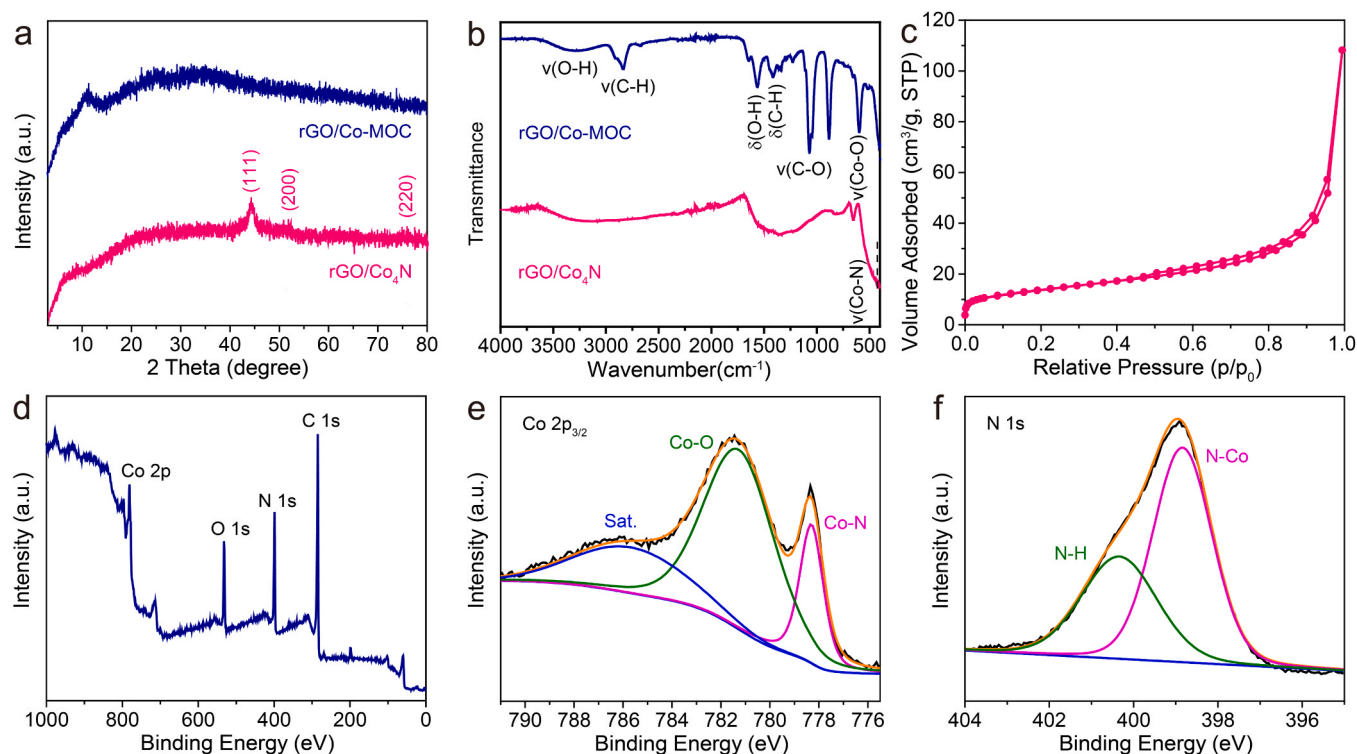
Fig. 2. (a) XRD patterns and (b) FTIR spectra of the rGO/Co-MOC and rGO/Co$_4$N. (c) N$_2$ adsorption-desorption isotherm of the rGO/Co$_4$N. XPS analysis of the rGO/Co$_4$N: (d) survey spectrum, (e) Co 2p, and (f) N 1s.

nanocomposite. The disappearance of the absorption peaks typical for the Co-MOC species in the FTIR spectrum of the rGO/Co$_4$N indicates the occurrence of full conversion of the rGO/Co-MOC precursor (Fig. 2b). Notably, the emergence of the peak at around 423 cm^{-1} attributed to Co-N stretching vibration further discloses the formation of Co nitride species [36]. Besides, as depicted the XRD pattern in Fig. 2a, the original peak at around 10° attributed to the rGO/Co-MOC precursor is no longer observable. Meanwhile, the diffraction peaks at 44.2°, 51.5°, and 75.9° can be indexed to the (111), (200), and (220) planes of the Co$_4$N with face centered cubic (*fcc*) phase, respectively, further evidencing the successful transformation to the rGO/Co$_4$N [37–39]. The SEM and TEM images with low magnifications in Fig. 1d–f exhibit 2D nanosheet morphology is retained well after nitridation treatment while the surface becomes much rougher. And the zoom-in TEM image (Fig. 1g) reveals that plentiful fine NPs (particle size = 15–18 nm) are uniformly immobilized on the surface of the 2D rGO. According to the HRTEM image presented in Fig. 1h, the fringes with a spacing of 0.21 nm, in line with the (111) plane of *fcc* phase Co$_4$N, can be clearly found [39]. This is in consistent with the aforementioned XRD characterization result (Fig. 2a). In addition, the EDX elemental mappings (Fig. 1i) from a single nanosheet further demonstrate the homogeneous distribution of the Co, N, and C elements, implying that Co$_4$N NPs with high-density are well-dispersed on the rGO nanosheet. And from the ICP-AES analysis, the content of Co in the rGO/Co$_4$N is about 70.0 wt%. Moreover, according to the N$_2$ adsorption-desorption measurement (Fig. 2c and S1), the BET specific surface area and the total pore volume of the rGO/Co$_4$N are determined to be 50.0 m^2/g and 0.17 cm^3/g, respectively, and the average pore size is centered at ca. 4.0 nm. Of note, the isotherm of the rGO/Co$_4$N features type IV one together with a type-H3 hysteresis loop ($P/P_0 > 0.5$), which is indicative of the slit-shaped mesoporous structure. From the above characterizations, such desirable special architectural features with high-density fine Co$_4$N NPs anchored on the thin rGO nanosheet, together with relatively large surface area and abundant pore structure, would endow the rGO/Co$_4$N nanocomposite with great potential for high-performance catalysis.

To obtain the surface composition and charge state of the rGO/Co$_4$N nanocomposite, the XPS analysis was also carried out. The survey spectrum in Fig. 2d further verifies the presence of the Co, N, and C elements in the sample. In the Co 2p spectrum (Fig. 2e), the peak at 778.3 eV is corresponded to Co-N species, and the peak at 781.4 eV is assigned to oxidized Co species because of superficial oxidation [39,40]. In the N 1s spectrum (Fig. 2f), the peak at 398.4 eV is corresponded to N−Co species, and the peak at 400.3 eV is for N-H species [39]. Obviously, above XPS result further suggests the successful generation of Co nitride species in the nitridation product.

For the sake of comparison, control samples with similar nanosheet morphology including air-calcination-derived rGO/Co$_3$O$_4$ and thermal-reduction-derived rGO/Co were prepared (Scheme 1). Additionally, the free-standing Co$_4$N without rGO substrate and pure rGO without Co$_4$N species were also included. Their synthetic details are listed in Experimental Section. The XRD and TEM techniques were conducted to investigate their structural and morphological information. The XRD patterns presented in Fig. 3a confirm the generation of spinel phase Co$_3$O$_4$ (PDF card no. 29-0497) in the rGO/Co$_3$O$_4$, *fcc* phase Co (PDF card no. 29-0497) in the rGO/Co, and *fcc* phase Co$_4$N in the free-standing Co$_4$N. The TEM images display that both rGO/Co$_3$O$_4$ and rGO/Co possess similar morphology with the rGO/Co$_4$N (Fig. 3b, c), and the pure rGO is thin nanosheets with smooth surface (Fig. 3d), assembling the pristine GO nanosheets. Besides, it is noteworthy that the free-standing Co$_4$N is composed of irregular aggregated particles (Fig. 3e). The above contrasting morphology with that of the rGO/Co$_4$N implies the critical role of GO incorporation for directing the generation 2D nanosheet morphology with fine Co$_4$N NPs immobilization, which is particularly desirable for active sites exposure and mass transportation during catalysis.

3.2. Catalytic performance investigation

4-chlorophenol (4-CP) was selected as the model organic pollutant to investigate the catalytic performance of the rGO/Co$_4$N nanocomposite
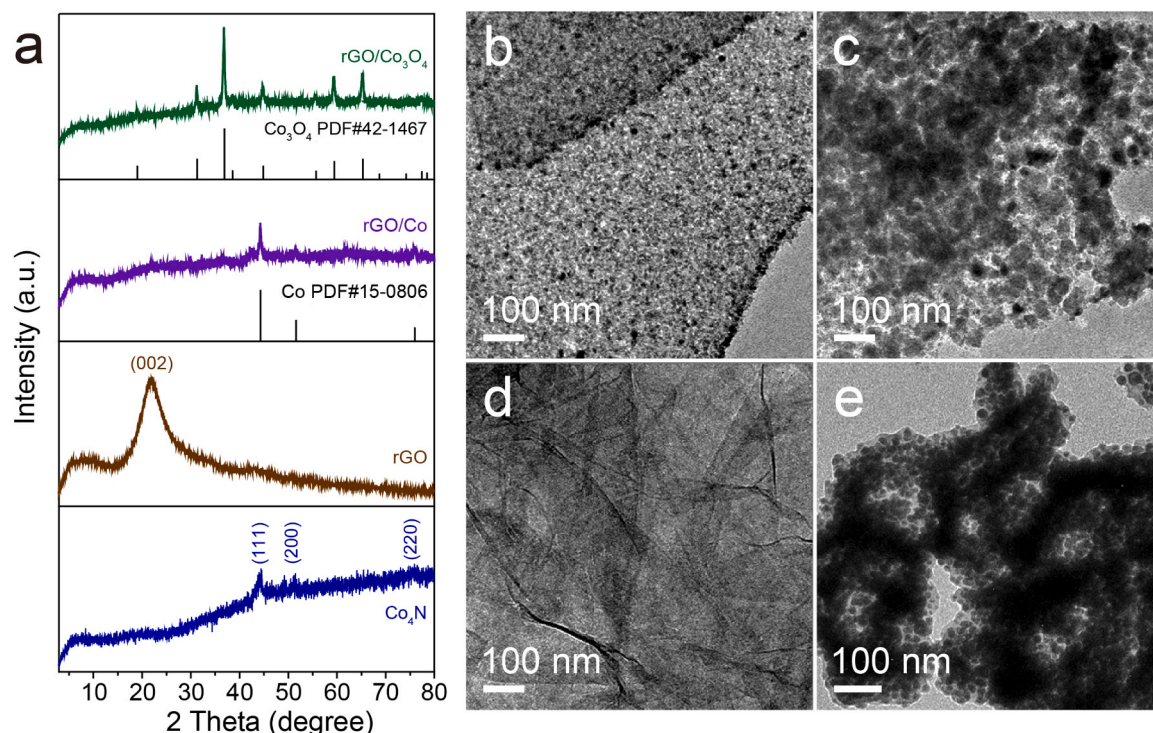
Fig. 3. (a) XRD patterns and TEM images of (b) rGO/Co$_3$O$_4$, (c) rGO/Co, (d) rGO, and (e) free-standing Co$_4$N.

acting as the PMS activator in SR-AOPs. For comparison purpose, the catalytic properties of the set of control samples were evaluated with using the same reaction conditions. As demonstrated in Fig. 4a, with only PMS adding, almost no 4-CP degradation occurs, indicating self-decomposition of PMS to release ROS is negligible. When only the rGO/Co$_4$N itself is added in 4-CP solution, only 0.1% of 4-CP can be removed through surface adsorption. Encouragingly, rGO/Co$_4$N can present excellent catalytic oxidative degradation activity in the presence of PMS, and 100% of 4-CP is fully degraded within the period of 20 min. By contrast, the control samples, free-standing Co$_4$N without rGO and pure rGO without Co$_4$N, exhibit much inferior catalytic activities, only 88.9% and 12.2% of 4-CP are eliminated within the period of 20 min, respectively.

For better comparison, the apparent rate constant (k) for catalytic degradation is analyzed via first-order kinetic model [ln(C$_t$/C$_0$) = - kt]. As reported in Fig. 4b and Table S1, the k of rGO/Co$_4$N is determined to be 0.682 min^{-1}, much larger than those of rGO (0.007 min^{-1}) and Co$_4$N (0.119 min^{-1}). Herein the superiority of the rGO/Co$_4$N to the free-standing Co$_4$N in catalytic 4-CP degradation can be attributed to its morphological and compositional advantages. On the one hand, with respect to the free-standing Co$_4$N displaying irregular and aggregated particles, high density and fine Co$_4$N NPs are uniformly immobilized on rGO surface, rendering rGO/Co$_4$N with maximized catalytic center exposure and promoted mass transfer for high-efficiency catalysis. On the other hand, with conductive rGO scaffold incorporation, the charge transfer can be promoted, thus further boosting PMS activation.

To highlight the advantage of Co$_4$N species for PMS activation, we further compare the catalytic behavior of rGO/Co$_4$N with those of the air-calcination-derived rGO/Co$_3$O$_4$ and reduction-derived rGO/Co with similar 2D nanosheet morphology. As depicted in Fig. 4c, d and Table S1, rGO/Co$_3$O$_4$ and rGO/Co display the 4-CP degradation efficiencies of 10.3% and 82.4%, with k values of 0.016 and 0.274 min^{-1}, respectively. Obviously, the two samples underperform the rGO/Co$_4$N for oxidative degradation of 4-CP. Considering the similar morphological structures of these rGO-supported nanocomposites while variations in Co-based moieties, the above contrasting results suggest the superior

intrinsic catalytic activity of Co$_4$N species to those of Co$_3$O$_4$ and metallic Co species. This phenomenon can be interpreted by the different local coordination environments and electronic structures of the active Co sites in these samples, which will be further elucidated in the later part. In addition, the widely-used benchmark Co$_3$O$_4$ was also studied. As indicated, 9.9% of 4-CP is removed within the period of 20 min by the Co$_3$O$_4$, which is much inferior to the rGO/Co$_4$N as well as other rGO-supported nanocomposites in this study. The above catalytic property evaluations disclose that Co$_4$N-based material is a class of promising and powerful catalysts for eliminating organic contaminants via PMS activation. And again, our exploration on the rGO/Co$_4$N illuminates that elegant innovation over the catalytic material presents an effective avenue to further boost the catalytic performance to a higher new level.

Moreover, impact of the reaction temperature on 4-CP removal by the rGO/Co$_4$N via PMS activation was evaluated. As indicated in Fig. 5a, with increasing temperature, degradation efficiency improves accordingly. This phenomenon could be interpreted by promoted thermal activation of PMS, and meanwhile, when lifting reaction temperature, more energy would input into the system, thereby facilitating crossing the reaction energy barrier. Specifically, the k values for the reactions at 20, 30, and 40 °C are determined to be 0.266, 0.376, and 0.540 min^{-1}, respectively (Fig. 5b). And the reaction activation energy (E$_a$) of the rGO/Co$_4$N is calculated to be 27.0 kJ mol^{-1} on the basis of the Arrhenius plot (lnk = -E$_a$/RT + lnA) (Fig. 5c), which is lower than those reported previously [41–43], indicating that the rGO/Co$_4$N have a significant catalytic activation in degradation of 4-CP.

To identify the general applicability of the rGO/Co$_4$N + PMS system, other organic contaminants with different molecular structures, i.e., BPA, FF, and IBP, were catalytically degraded as model pollutants. Impressively, as presented in Fig. 5d–f, rGO/Co$_4$N could exhibit outstanding catalytic degradation activities for all these three organic pollutants. In detail, 99.8% of the BPA, 98.1% of the FF, and 99.9% of the IBP can be eliminated within 20 min by the catalysis of rGO/Co$_4$N. Of note, these catalytic degradation efficiencies are much higher than those of the benchmark Co$_3$O$_4$, with which only 49.8% of the BPA, 16.7% of the FF, and 13.7% of the IBP can be eliminated during the same
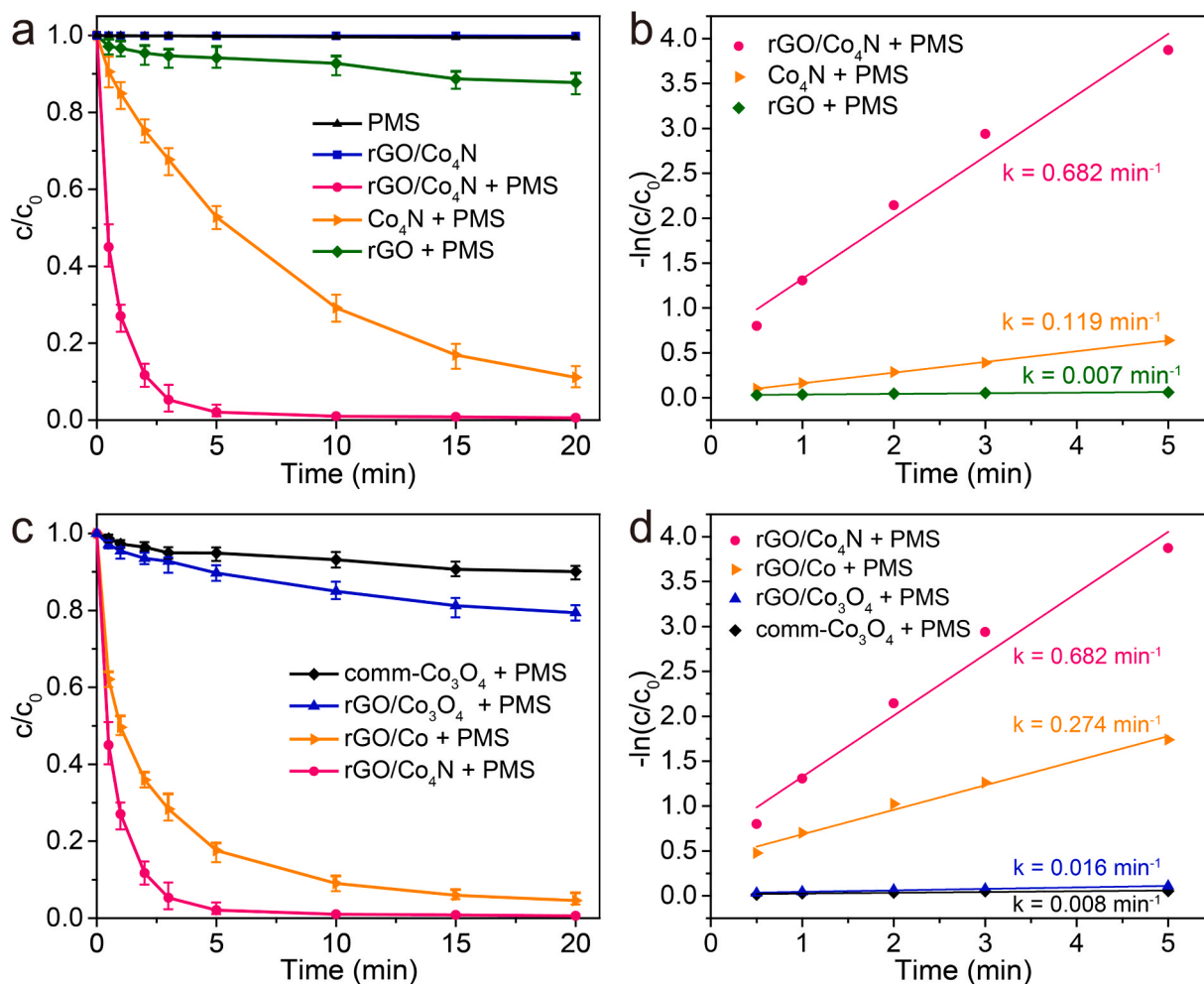
Fig. 4. (a,c) 4-CP degradation profiles, and (b,d) the corresponding reaction rate constants of different systems. Reaction condition: [4-CP] = 50 mg/L, [catalyst] = 50 mg/L, [PMS] = 200 mg/L, T = 20 °C.

reaction time period.

Furthermore, the stability of the rGO/Co$_4$N for 4-CP removal through activation of PMS was studied. As shown in Fig. 6a, for the first consecutive 3 cycles, the 4-CP degradation efficiency can maintain up to 98% within 20 min. And the 4-CP degradation efficiencies decrease slightly for the next two cycles, yet can still retain at about 84%, suggesting the respectable stability of the rGO/Co$_4$N as the PMS activator for 4-CP elimination. The reason for the decreased catalytic performance in the reusability evaluation can be probably explained by the coverage of intermediate species on the surface of rGO/Co$_4$N, blocking the catalytic centers in some degree. In addition, The TEM and XRD techniques were also carried out on the spent rGO/Co$_4$N. As indicated in Fig. 6b, the morphology is largely retained, further signifying the robustness of the rGO/Co$_4$N. Of note, in the XRD pattern of the used rGO/Co$_4$N (Fig. 6c), two weak peaks at 36.8° and 65.2° ascribed to the (311) and (400) planes of the spinel phase Co$_3$O$_4$ emerge, indicating the occurrence of slight oxidization of Co$_4$N species under such highly oxidizing condition. Also, the partial oxidation of Co$_4$N species is probably another reason for the decreased catalytic activity of rGO/Co$_4$N after multiple cycles. Further improvement of the catalytic stability of the rGO/Co$_4$N is necessary to enable its wide application in SR-AOPs, which will be the focus in our future work.

3.3. ROS and catalytic active centers identification

In order to identify ROS generated in rGO/Co$_4$N + PMS system,

radical scavenger experiment was conducted. In general, ROS such as SO$_4^{•-}$, •OH, O$_2^{•-}$, and ^{1}O$_2$ are conventionally involved in PMS activation [8,9]. Herein, TBA and MeOH radical scavengers were selected to determine roles of •OH and SO$_4^{•-}$ [9,44,45]. Additionally, scavenging agents p-BQ and NaN$_3$ were used for detection of O$_2^{•-}$ and ^{1}O$_2$, respectively [44–46]. From the results illustrated in Fig. 7a, it can be found that the degradation efficiencies of 4-CP decline from 100% to 95.2% and 55.3% within 20 min when adding TBA and MeOH in the reaction system, respectively, implying that both •OH and SO$_4^{•-}$ are the reactive species for 4-CP removal. Besides, only 80.0% and 24% of the 4-CP are removed when adding p-BQ and NaN$_3$ in the reaction system, respectively, indicating that O$_2^{•-}$ and ^{1}O$_2$ are also involved in the activation of PMS. Collectively, according to the quenching experiment, SO$_4^{•-}$, •OH, O$_2^{•-}$, and ^{1}O$_2$ were generated for 4-CP removal by rGO/-Co$_4$N via PMS activation.

Further, the EPR experiments were conducted for probing ROS involved with DMPO and TEMP acting as the spin-trapping reagents. In particular, DMPO was added in deionized water system to identify the presence of •OH and SO$_4^{•-}$ [45,47]. As depicted in Fig. 7b, a narrow seven-line spectrum (1:2:1:2:1:2:1), which corresponds to DMPOX (the oxidation product of DMPO), can be observed in the co-presence of rGO/Co$_4$N and PMS, suggesting DMPO would be easily oxidized by the oxidizing species (eg., •OH and SO$_4^{•-}$) instead of combining with the above species to generate the adducts DMPO−•OH and DMPO−SO$_4^{•-}$ [48,49]. Additionally, Fig. 7c exhibits a distinct characteristic signal for DMPO−O$_2^{•-}$ adduct when rGO/Co$_4$N, PMS and DMPO were added in
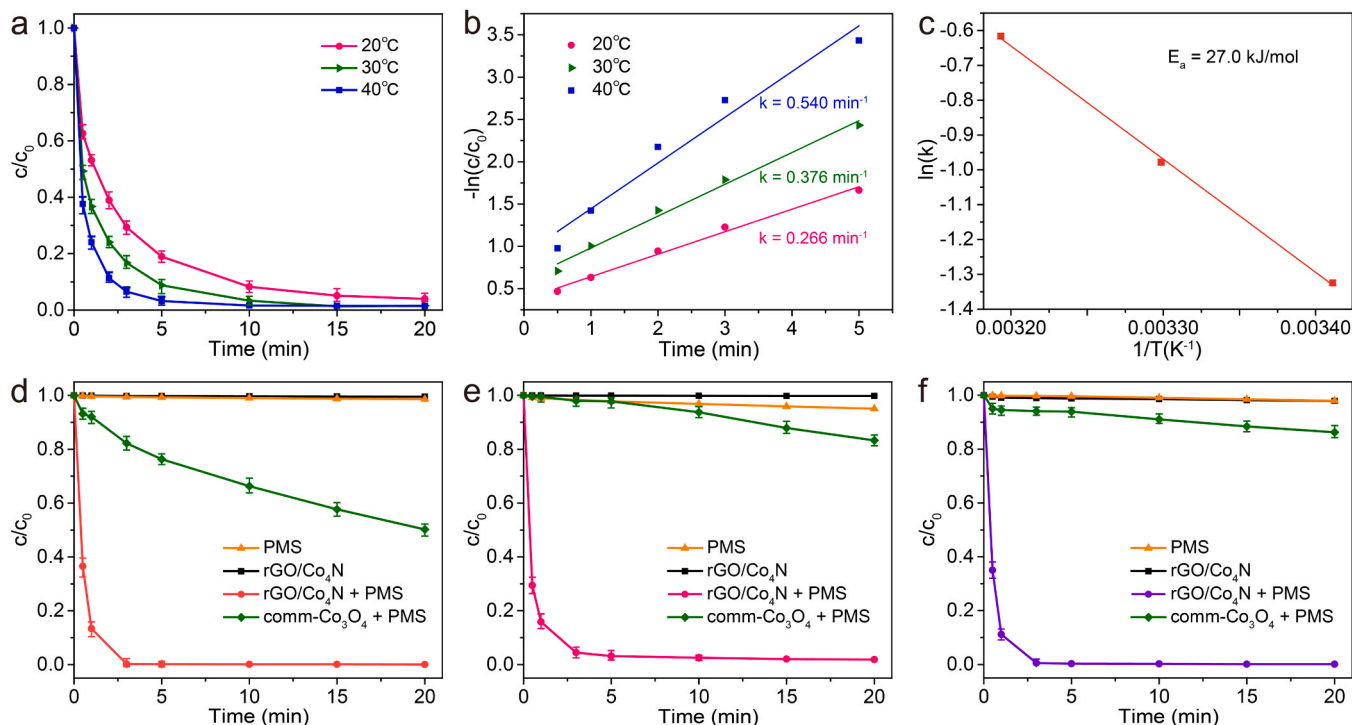
Fig. 5. (a) Impact of reaction temperature on 4-CP degradation, (b) the corresponding reaction rate constants, and (c) the Arrhenius plot over the rGO/Co₄N. Catalytic degradation investigations of other model organic pollutants: (d) bisphenol A (BPA), (e) florfenicol (FF), and (f) ibuprofen (IBP). Reaction condition: [catalyst] = 50 mg/L, [PMS] = 200 mg/L, [4-CP] = 60 mg/L (for a), [BPA] = 25 mg/L (for d), [FF] = 20 mg/L (for e), [IBP] = 20 mg/L (for f), T = 20 °C (for d, e, and f).
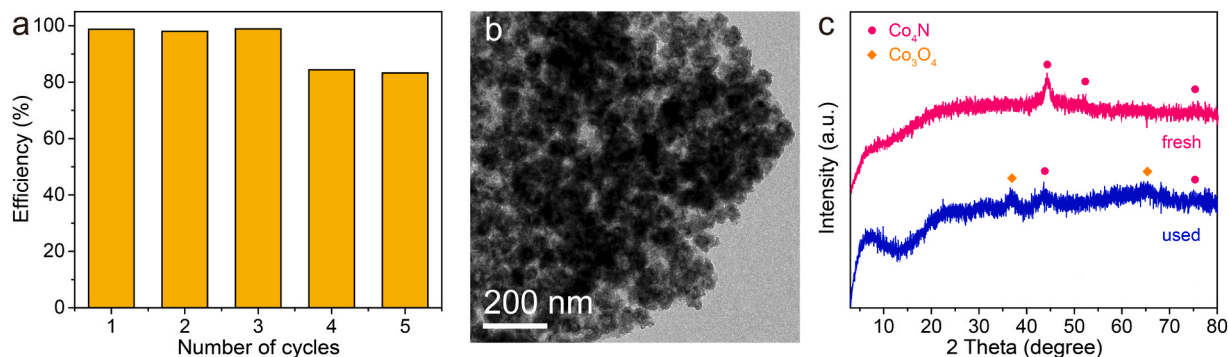

Fig. 6. (a) The reusability test of the rGO/Co₄N for catalytic 4-CP degradation. Reaction condition: [catalyst] = 50 mg/L, [PMS] = 200 mg/L, [4-CP] = 50 mg/L, initial pH = 7.5, T = 20 °C. The characterizations of the spent rGO/Co₄N: (b) TEM image and (c) XRD pattern.

MeOH solution system [50]. Furthermore, when employing TEMP to capture $^1O_2$ in deionized water system, a characteristic triplet signal (1:1:1) of the TEMP−$^1O_2$ can be detected [51–53], indicating the generation of $^1O_2$ during PMS activation by the rGO/Co₄N (Fig. 7d). Notably, in the absence of the rGO/Co₄N, no significant signal can be observed in the EPR spectra, revealing that the self-decomposition of PMS is negligible (Fig. 7b–d). To summarize, our rGO/Co₄N nanocomposite plays a crucial role in catalytic PMS activation, which can produce various ROS, including •OH, SO₄•⁻, O₂•⁻ and $^1O_2$, for the organic pollutant degradation.

To illuminate the mechanism of PMS activation over the rGO/Co₄N nanocomposite, XPS analysis was performed on the used rGO/Co₄N after catalysis. The Co 2p spectrum of the spent rGO/Co₄N is displayed in Fig. 8a, it can be found that in comparison with the fresh sample, the relative content of the Co–O species increase accompanied by the decrease of the Co–N species in intensity, suggesting that partial conversion of Co–N to Co–O species. In other words, the redox cycles of the

Co species are involved during the PMS activation catalyzed by the rGO/Co₄N. In the N 1s spectra (Fig. 8b), the emerged weak peak at 404.0 eV can be associated with the N–O species [54,55], suggesting the happening of the oxidation of the rGO/Co₄N during the catalytic process.

3.4. Mechanism study on promoted catalytic performance

The superior catalytic property of rGO/Co₄N in comparison with the controls in this work can be attributed to special chemical compositional, morphological, and structural characteristics. Firstly, different from free-standing Co₄N control with serious agglomeration of numerous NPs, in the rGO/Co₄N composite, the rGO substrate can well disperse high-density Co₄N NPs to generate the 2D nanosheet morphology with high surface area and rich pore structure, thus rendering better exposure of catalytic centers and efficient mass transfer. Besides, it is known that good electron transfer behavior can
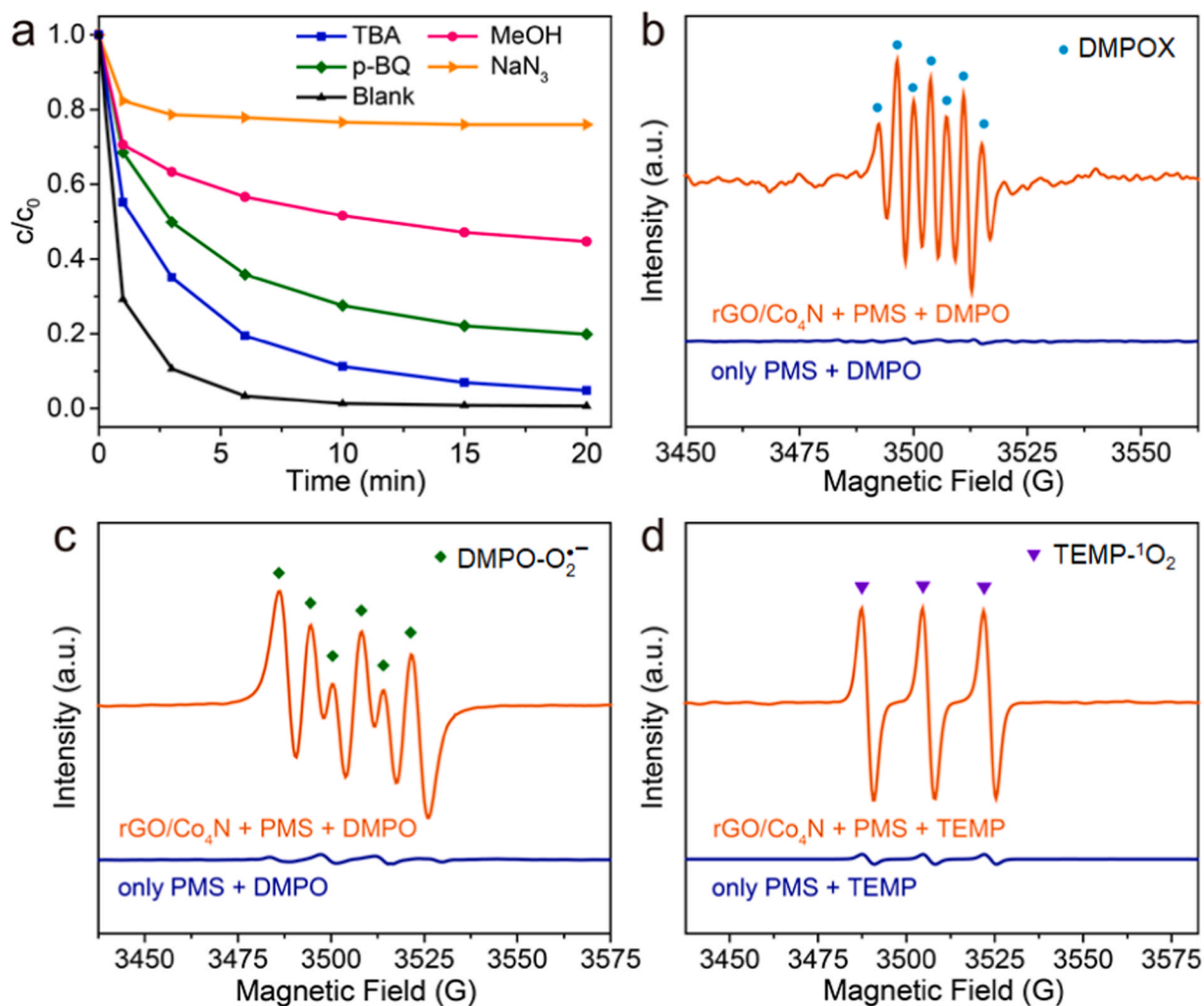
Fig. 7. (a) Radical quenching studies on 4-CP degradation by rGO/Co$_4$N. EPR spectra in the presence of (b) DMPO (solvent: deionized water), (c) DMPO (solvent: MeOH), and (d) TEMP. Reaction condition: [catalyst] = 50 mg/L, [PMS] = 200 mg/L, [4-CP] = 50 mg/L, [MeOH] = 200 mM, [TBA] = 200 mM, [NaN$_3$] = 1 mM, [p-BQ] = 1 mM, [DMPO] = 150 mM, [TEMP] = 150 mM, T = 20 °C.
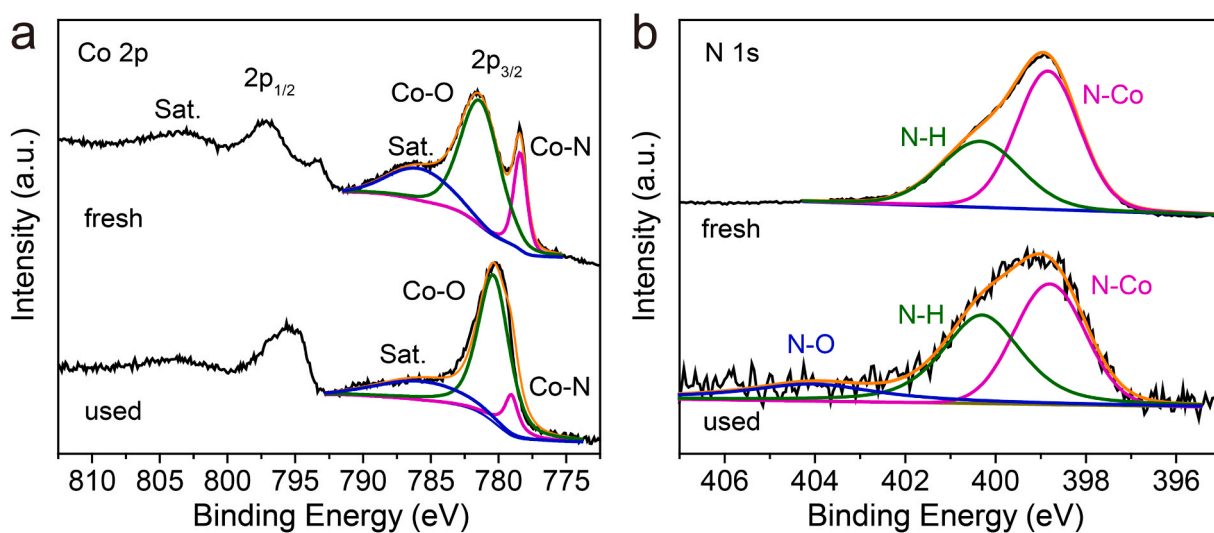

Fig. 8. XPS spectra for the fresh and spent rGO/Co$_4$N: (a) Co 2p and (b) N 1s.

promote PMS activation [17,56,57]. Obviously, in our rGO/Co$_4$N, the conductive rGO scaffold would effectively accelerate the charge transfer process to enable boosted PMS activation. More significantly, Co$_4$N possesses intrinsically metallic property, that is, Co$_4$N in itself is a good conductor for smooth electron transfer, which is in sharp contrast with the semiconductor Co$_3$O$_4$ [32,37]. To testify the above claim, the electrochemical impedance spectroscopy (EIS) analysis was further carried out to evaluate the electrical properties of rGO/Co$_4$N together with the free-standing Co$_4$N and rGO/Co$_3$O$_4$ controls. From the Nyquist plots in Fig. S2, it can be observed that the arc size of these three samples increase with the following order: rGO/Co$_4$N < Co$_4$N < rGO/Co$_3$O$_4$, demonstrating that the lowest charge transfer resistance (R$_{ct}$) of the rGO/Co$_4$N. The result indicates that the rGO/Co$_4$N sample has better charge transfer capacity and higher electron transfer efficiency relative to both free-standing Co$_4$N and rGO/Co$_3$O$_4$ samples, suggesting that the conductive rGO substrate and the Co$_4$N species with excellent intrinsic conductivity synergistically endow the rGO/Co$_4$N composite with excellent electrical conductivity to substantially promote the electron transportation for PMS activation.

Furthermore, density functional theory (DFT) calculations were conducted to elaborate the superiority of the Co$_4$N species to the conventional activators such as metallic Co and Co$_3$O$_4$ for PMS activation. The density of states (DOS) in Fig. 9a–c clearly show that the above three samples possess varied electronic structures, both Co$_4$N and Co have higher DOS near the Fermi level than the Co$_3$O$_4$, indicating good conductivity of Co and Co$_4$N. Obviously, such conductive feature is desirable for the charge transport during PMS activation.

Fig. 9d, e, g and h illustrate the optimized configurations of the PMS adsorbed on the Co$_4$N (111), Co$_3$O$_4$ (110) and Co (111) model surfaces. It is well-adopted that a typical heterogeneous PMS activation involves PMS adsorption, electron transfer from the catalyst to PMS, and PMS decomposition via the O–O bond cleavage [18,30,58]. Based on the above considerations, the length of the O–O bond (l$_{O-O}$), the adsorption energy of PMS (E$_{ads}$), and the number of charge transfer between the catalyst and PMS (Q$_{ct}$) were calculated and summarized in Table S2. As demonstrated, compared with the l$_{O-O}$ of original free PMS (1.342 Å),
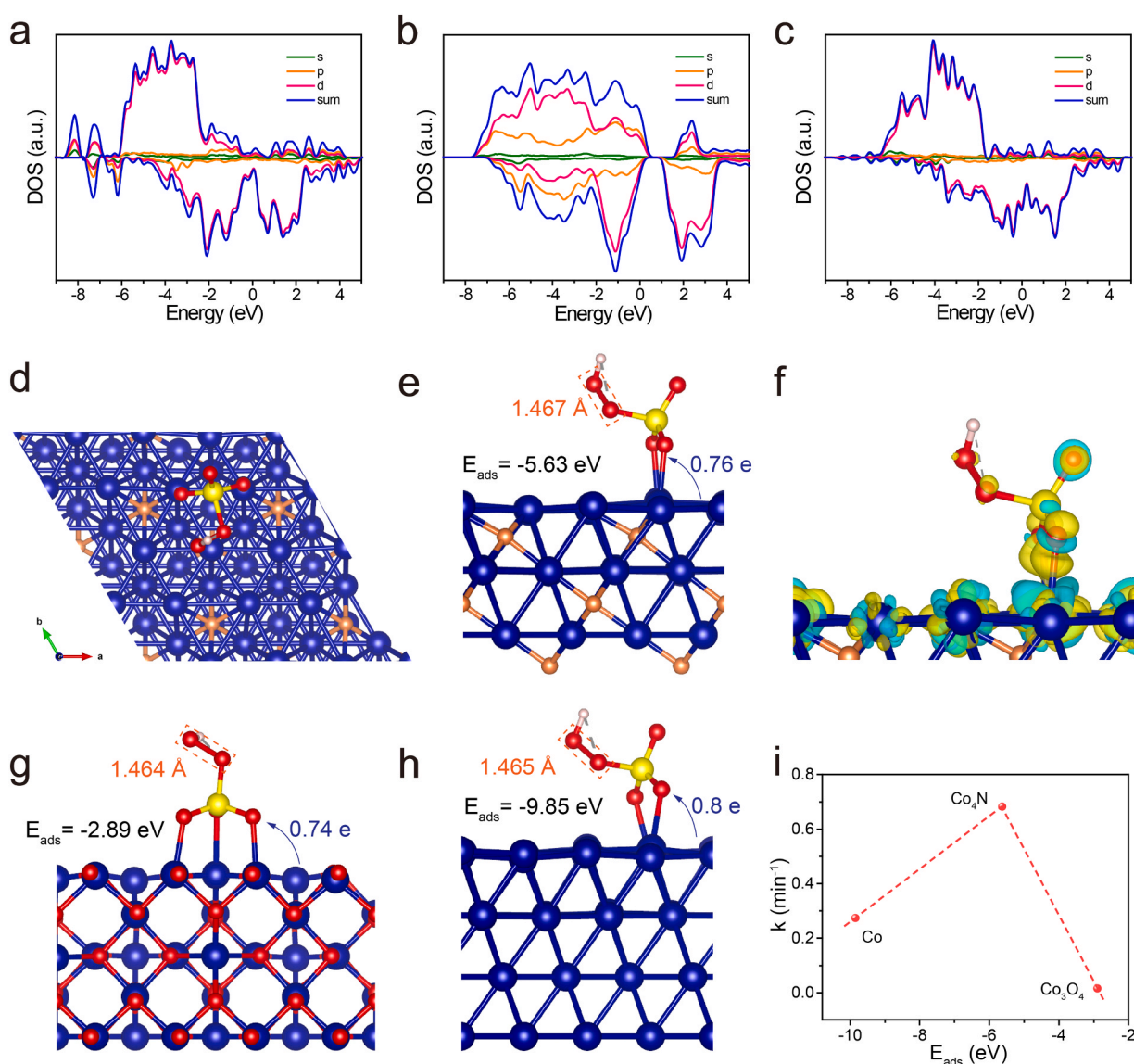

Fig. 9. Calculated density of states (DOS) of (a) Co$_4$N (111) surface, (b) Co$_3$O$_4$ (110) surface and (c) Co (111) surface. The geometric configurations of PMS adsorption on Co$_4$N (111) surface: (d) top view and (e) side view. (f) Charge density difference analysis on the Co$_4$N (111) + PMS system. Yellow denotes electron accumulation and cyan denotes electron depletion. The geometric configurations of PMS adsorption on (g) Co$_3$O$_4$ (110) surface and (h) Co (111) surface. (i) Catalytic activity over different samples as a function of the adsorption energy of PMS (E$_{ads}$). The orange, blue, pink, yellow, and red spheres refer to the N, Co, H, S and O atoms, respectively. (For interpretation of the references to color in this figure legend, the reader is referred to the web version of this article.)

the l_{O-O} of the adsorbed PMS on the Co$_4$N (111), Co$_3$O$_4$ (110) and Co (111) model surfaces are lengthened to 1.467, 1.464 and 1.465 Å, respectively, indicating the adsorbed PMS is ready to be activated and cleaved. Additionally, the PMS adsorption on the Co$_4$N (111) surface is moderate (E$_{ads}$ = −5.63 eV), that is, stronger than on the Co$_3$O$_4$ (110) surface (E$_{ads}$ = −2.89 eV) while weaker than on the Co (111) surface (E$_{ads}$ = −9.85 eV). Intriguingly, it is found that the reaction rate of the catalyst for catalyzing 4-CP degradation can be correlated with the E$_{ads}$ of the PMS via a volcano-type relationship (Fig. 9i). This trend can be interpreted with the classical Sabatier principle [59,60]. Too strong binding strength of the PMS would lead to the catalyst poisoning, while too weak binding would be inadequate to activate the PMS. In other words, the moderate adsorption of the PMS is optimal for triggering its activation. Obviously, in our study, Co$_4$N (111) surface with a modest PMS adsorption strength is more favorable for catalytic 4-CP degradation via activation of PMS. Besides, charge density difference analysis was performed on Co$_4$N (111) + PMS system and illustrated in Fig. 9f. It can be clearly observed the charge accumulation on the PMS and the charge depletion on the Co$_4$N (111), that is, the presence of electron transfer from the Co$_4$N (111) to PMS molecule, further suggesting that Co$_4$N is more preferable for activating PMS to release ROS.

With the above investigations, the degradation mechanism for 4-CP by the rGO/Co$_4$N via PMS activation could be presented in Fig. 10. In brief, PMS diffuses to close to the rGO/Co$_4$N. Then PMS is adsorbed on the rGO/Co$_4$N accompanied by charge transfer, leading to effective activation to generate various ROS, and thereby degrading the organic pollutant. Of note, the rGO/Co$_4$N, possessing high density and fine Co$_4$N NPs homogeneously functionalized on the surface of rGO nanosheets, is favorable for catalytic site exposure and mass transfer. Meanwhile, the presence of conductive rGO would be conducive to charge transfer process for catalysis. Significantly, owing to the effective modulation by the nonmetal N coordination, the Co$_4$N moieties in the rGO/Co$_4$N possess desirable atomic coordination environment and electronic state, thus affording optimal binding strength for PMS activation.

Specifically, the mechanism for PMS activation over rGO/Co$_4$N can be summarized as follows based on our experiments together with previous accounts [16, 30, 45, 61–63]. Firstly, the Co^0 in the rGO/Co$_4$N can activate PMS to produce SO$_4^{•−}$ and •OH, and meanwhile, Co^0 in itself would be oxidized to Co^{2+} and Co^{3+} (Eqs. 1 and 2). Next, the generated Co^{2+} can continuously react with PMS to produce SO$_4^{•−}$ along with the conversion to Co^{3+} (Eq. 3). On the other hand, both PMS and Co^0 can reduce Co^{3+} to Co^{2+} (Eqs. 4 and 5), thus ensuring the catalytic reaction can proceed cyclically. Besides, combined with the previous reports, the electron-rich ketone groups and defect sites on rGO surface could also activate PMS to yield •OH and SO$_4^{•−}$. Additionally, •OH can originate from the reaction between SO$_4^{•−}$ and H$_2$O (Eq. 6). O$_2^{•−}$ can be generated from the dissolved oxygen via one-electron reduction process (Eq. 7), and further, ^{1}O$_2$ can be produced from the O$_2^{•−}$ recombination process (Eqs. 8–10).
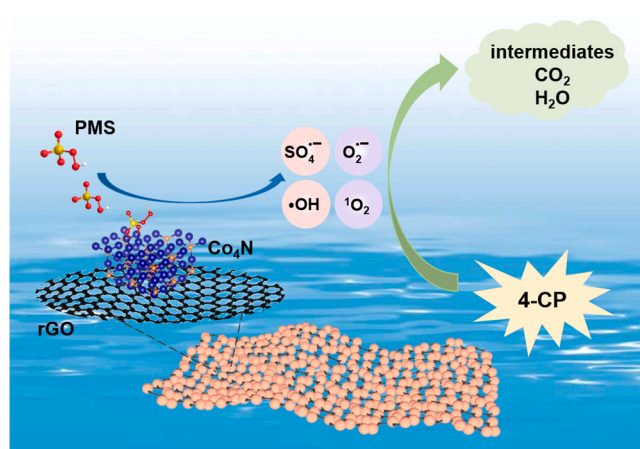
$$Co^0 + 2HSO_5^- \rightarrow Co^{2+} + 2SO_4^{•-} + 2OH^- \qquad (1)$$

$$Co^0 + 3HSO_5^- \rightarrow Co^{3+} + 3SO_4^{•-} + 3•OH \qquad (2)$$

$$Co^{2+} + HSO_5^- \rightarrow Co^{3+} + SO_4^{•-} + OH^- \qquad (3)$$

$$Co^{3+} + HSO_5^- \rightarrow Co^{2+} + SO_5^{•-} + H^+ \qquad (4)$$

$$2Co^{3+} + Co^0 \rightarrow 3Co^{2+} \qquad (5)$$

$$SO_4^{•-} + H_2O \rightarrow SO_4^{2-} + H^+ + •OH \qquad (6)$$

$$O_2 + e^- \rightarrow O_2^{•-} \qquad (7)$$

$$O_2^{•-} + H_2O \rightarrow HOO• + OH^- \qquad (8)$$

$$O_2^{•-} + HOO• \rightarrow {}^1O_2 + HOO^- \qquad (9)$$

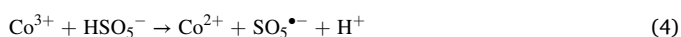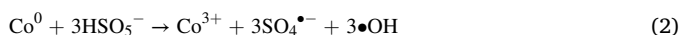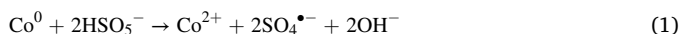$$HOO• + HOO• \rightarrow {}^1O_2 + H_2O_2 \qquad (10)$$

Fig. 10. Activation of PMS by the rGO/Co$_4$N nanocomposite for catalytic 4-CP degradation.

4. Conclusion

In summary, we report, for the first time, the construction of the rGO/Co$_4$N nanocomposite via a sustainable and facile MOC-mediated method with the assistance of the urea for boosted PMS activation in SR-AOPs. The rGO/Co$_4$N nanocomposite, with high density and fine Co$_4$N NPs loaded on the rGO nanosheets, is beneficial for catalytic site exposure, improved robustness as well as rapid mass transfer during catalysis. Meanwhile, the incorporated conductive rGO scaffold could accelerate the charge transfer. Intriguingly, as revealed from the DFT calculations, owing to the effective electronic modulation by the nonmetal N incorporating into the interstices of the Co framework, the Co$_4$N could possess more desirable electronic state with respect to the common Co$_3$O$_4$ and metallic Co for the PMS adsorption and decomposition. As a result, the rGO/Co$_4$N nanocomposite performs as an excellent heterogeneous catalyst for degrading organic pollutants via PMS activation, considerably surpassing other Co-based catalysts supported by the rGO (rGO/Co$_3$O$_4$ and rGO/Co). Particularly, when using 4-CP as the model pollutant, up to 42 times of catalytic efficiency boost is yielded for rGO/Co$_4$N (0.682 min^{-1}) relative to rGO/Co$_3$O$_4$ (0.016 min^{-1}). In addition, the catalytic active centers of rGO/Co$_4$N as well as the involved ROS are systematically investigated and identified. This study illuminates that TMN hold great potential in SR-AOPs, the rGO/Co$_4$N presented herein would enrich the catalyst family for PMS activation and inspire more novel catalyst engineering. Further, it is demonstrated that elegant manipulation over the morphological structure and local atom coordination environment of the catalyst is highly promising to achieve high-performance catalysis for AOPs and beyond.

CRediT authorship contribution statement

Ping Li: Conceptualization, Project administration, Writing – review & editing, Supervision, Funding acquisition. **Yunan Lin:** Methodology, Investigation, Resources, Formal analysis, Visualization, Data curation, Writing – original draft. **Quhua Huang:** Formal analysis, Data curation, Validation, Writing – review & editing. **Wenqin Li:** Resources, Validation. **Shien Zhao:** Resources, Data curation. **Yi Fu:** Data curation, Validation. **Feng Chu:** Data curation, Validation. **Shuanghong Tian:** Project administration, Writing – review & editing.

Declaration of Competing Interest

The authors declare that they have no known competing financial interests or personal relationships that could have appeared to influence

the work reported in this paper.

Acknowledgements

Appendix A. Supporting information

Supplementary data associated with this article can be found in the online version at doi:10.1016/j.apcatb.2021.120850.

References

[1] K.E. O'Shea, D.D. Dionysiou, Advanced oxidation processes for water treatment, J. Phys. Chem. Lett. 3 (2012) 2112–2113, https://doi.org/10.1021/jz300929x.
[2] G. Zhan, H.C. Zeng, Charge-switchable integrated nanocatalysts for substrate-selective degradation in advanced oxidation processes, Chem. Mater. 28 (2016) 4572–4582, https://doi.org/10.1021/acs.chemmater.6b01128.
[3] K.H.H. Aziz, H. Miessner, S. Mueller, D. Kalass, D. Moeller, I. Khorshid, M.A. M. Rashid, Degradation of pharmaceutical diclofenac and ibuprofen in aqueous solution, a direct comparison of ozonation, photocatalysis, and non-thermal plasma, Chem. Eng. J. 313 (2017) 1033–1041, https://doi.org/10.1016/j.cej.2016.10.137.
[4] D.B. Miklos, C. Remy, M. Jekel, K.G. Linden, J.E. Drewes, U. Hübner, Evaluation of advanced oxidation processes for water and wastewater treatment – a critical review, Water Res. 139 (2018) 118–131, https://doi.org/10.1016/j.watres.2018.03.042.
[5] D. Ma, H. Yi, C. Lai, X. Liu, X. Huo, Z. An, L. Li, Y. Fu, B. Li, M. Zhang, L. Qin, S. Liu, L. Yang, Critical review of advanced oxidation processes in organic wastewater treatment, Chemosphere 275 (2021), 130104, https://doi.org/10.1016/j.chemosphere.2021.130104.
[6] Y. Shang, X. Xu, B. Gao, S. Wang, X. Duan, Single-atom catalysis in advanced oxidation processes for environmental remediation, Chem. Soc. Rev. 50 (2021) 5281–5322, https://doi.org/10.1039/D0CS01032D.
[7] F. Ghanbari, M. Moradi, Application of peroxymonosulfate and its activation methods for degradation of environmental organic pollutants: review, Chem. Eng. J. 310 (2017) 41–62, https://doi.org/10.1016/j.cej.2016.10.064.
[8] J. Wang, S. Wang, Activation of persulfate (PS) and peroxymonosulfate (PMS) and application for the degradation of emerging contaminants, Chem. Eng. J. 334 (2018) 1502–1517, https://doi.org/10.1016/j.cej.2017.11.059.
[9] J. Lee, U. von Gunten, J.H. Kim, Persulfate-based advanced oxidation: critical assessment of opportunities and roadblocks, Environ. Sci. Technol. 54 (2020) 3064–3081, https://doi.org/10.1021/acs.est.9b07082.
[10] U. Ushani, X. Lu, J. Wang, Z. Zhang, J. Dai, Y. Tan, S. Wang, W. Li, C. Niu, T. Cai, N. Wang, G. Zhen, Sulfate radicals-based advanced oxidation technology in various environmental remediation: a state-of-the–art review, Chem. Eng. J. 402 (2020), 126232, https://doi.org/10.1016/j.cej.2020.126232.
[11] S. Giannakis, K.-Y.A. Lin, F. Ghanbari, A review of the recent advances on the treatment of industrial wastewaters by sulfate radical-based advanced oxidation processes (SR-AOPs), Chem. Eng. J. 406 (2021), 127083, https://doi.org/10.1016/j.cej.2020.127083.
[12] G.P. Anipsitakis, D.D. Dionysiou, Radical generation by the interaction of transition metals with common oxidants, Environ. Sci. Technol. 38 (2004) 3705–3712, https://doi.org/10.1021/es035121o.
[13] J. Hou, X. He, S. Zhang, J. Yu, M. Feng, X. Li, Recent advances in cobalt-activated sulfate radical-based advanced oxidation processes for water remediation: a review, Sci. Total Environ. 770 (2021), 145311, https://doi.org/10.1016/j.scitotenv.2021.145311.
[14] Z.-S. Zhu, X.-J. Yu, J. Qu, Y.-Q. Jing, Y. Abdelkrim, Z.-Z. Yu, Preforming abundant surface cobalt hydroxyl groups on low crystalline flowerlike Co₃(Si₂O₅)₂(OH)₂ for enhancing catalytic degradation performances with a critical nonradical reaction, Appl. Catal. B 261 (2020), 118238, https://doi.org/10.1016/j.apcatb.2019.118238.
[15] P. Li, Y. Lin, S. Zhao, Y. Fu, W. Li, R. Chen, S. Tian, Defect-engineered Co₃O₄ with porous multishelled hollow architecture enables boosted advanced oxidation processes, Appl. Catal., B 298 (2021) 120596, https://doi.org/10.1016/j.apcatb.2021.120596.
[16] M. Zhang, C. Wang, C. Liu, R. Luo, J. Li, X. Sun, J. Shen, W. Han, L. Wang, Metal–organic framework derived Co₃O₄/C@SiO₂ yolk–shell nanoreactors with enhanced catalytic performance, J. Mater. Chem. A 6 (2018) 11226–11235, https://doi.org/10.1039/C8TA03565B.
[17] W.J. Tian, H.Y. Zhang, Z. Qian, T.H. Ouyang, H.Q. Sun, J.Y. Qin, M.O. Tade, S. B. Wang, Bread-making synthesis of hierarchically Co@C nanoarchitecture in heteroatom doped porous carbons for oxidative degradation of emerging contaminants, Appl. Catal. B 225 (2018) 76–83, https://doi.org/10.1016/j.apcatb.2017.11.056.
[18] X. Duan, J. Kang, W. Tian, H. Zhang, S.-H. Ho, Y.-A. Zhu, Z. Ao, H. Sun, S. Wang, Interfacial-engineered cobalt@carbon hybrids for synergistically boosted evolution of sulfate radicals toward green oxidation, Appl. Catal. B 256 (2019), 117795, https://doi.org/10.1016/j.apcatb.2019.117795.
[19] L. Peng, Y. Shang, B. Gao, X. Xu, Co₃O₄ anchored in N, S heteroatom co-doped porous carbons for degradation of organic contaminant: role of pyridinic N-Co binding and high tolerance of chloride, Appl. Catal. B 282 (2021), 119484, https://doi.org/10.1016/j.apcatb.2020.119484.
[20] Z.Y. Wang, L. Xu, F.Z. Huang, L.B. Qu, J.T. Li, K.A. Owusu, Z. Liu, Z.F. Lin, B. H. Xiang, X. Liu, K.N. Zhao, X.B. Liao, W. Yang, Y.B. Cheng, L.Q. Mai, Copper-nickel nitride nanosheets as efficient bifunctional catalysts for hydrazine-assisted electrolytic hydrogen production, Adv. Energy Mater. 9 (2019) 800, https://doi.org/10.1002/aenm.201900390.
[21] J. Zheng, X.L. Chen, X. Zhong, S.Q. Li, T.Z. Liu, G.L. Zhuang, X.N. Li, S.W. Deng, D. H. Mei, J.G. Wang, Hierarchical porous NC@CuCo nitride nanosheet networks: highly efficient bifunctional electrocatalyst for overall water splitting and selective electrooxidation of benzyl alcohol, Adv. Funct. Mater. 27 (2017) 11, https://doi.org/10.1002/adfm.201704169.
[22] H.P. Guo, B.Y. Ruan, W.B. Luo, J.Q. Deng, J.Z. Wang, H.K. Liu, S.X. Dou, Ultrathin and edge-enriched Holey nitride nanosheets as bifunctional electrocatalysts for the oxygen and hydrogen evolution reactions, ACS Catal. 8 (2018) 9686–9696, https://doi.org/10.1021/acscatal.8b01821.
[23] Z. Shen, Z. Zhang, M. Li, Y. Yuan, Y. Zhao, S. Zhang, C. Zhong, J. Zhu, J. Lu, H. Zhang, Rational design of a Ni₃N₀.₈₅ electrocatalyst to accelerate polysulfide conversion in lithium–sulfur batteries, ACS Nano 14 (2020) 6673–6682, https://doi.org/10.1021/acsnano.9b09371.
[24] Y. Zhong, X. Xia, F. Shi, J. Zhan, J. Tu, H.J. Fan, Transition metal carbides and nitrides in energy storage and conversion, Adv. Sci. 3 (2016), 1500286, https://doi.org/10.1002/advs.201500286.
[25] H. Wang, J. Li, K. Li, Y. Lin, J. Chen, L. Gao, V. Nicolosi, X. Xiao, J.-M. Lee, Transition metal nitrides for electrochemical energy applications, Chem. Soc. Rev. 50 (2021) 1354–1390, https://doi.org/10.1039/D0CS00415D.
[26] P. Li, R. Chen, S. Zhao, W. Li, Y. Lin, Y. Yu, Architecture control and electronic structure engineering over Ni-based nitride nanocomposite for boosting ammonia borane dehydrogenation, Appl. Catal. B 298 (2021), 120523, https://doi.org/10.1016/j.apcatb.2021.120523.
[27] H.-F. Wang, C. Tang, B.-Q. Li, Q. Zhang, A review of anion-regulated multi-anion transition metal compounds for oxygen evolution electrocatalysis, Inorg. Chem. Front. 5 (2018) 521–534, https://doi.org/10.1039/C7QI00780A.
[28] H. Jin, X. Liu, S. Chen, A. Vasileff, L. Li, Y. Jiao, L. Song, Y. Zheng, S.-Z. Qiao, Heteroatom-doped transition metal electrocatalysts for hydrogen evolution reaction, ACS Energy Lett. 4 (2019) 805–810, https://doi.org/10.1021/acsenergylett.9b00348.
[29] Y. Sun, T. Zhang, C. Li, K. Xu, Y. Li, Compositional engineering of sulfides, phosphides, carbides, nitrides, oxides, and hydroxides for water splitting, J. Mater. Chem. A 8 (2020) 13415–13436, https://doi.org/10.1039/D0TA05038E.
[30] X. Li, Z. Ao, J. Liu, H. Sun, A.I. Rykov, J. Wang, Topotactic transformation of metal–organic frameworks to graphene-encapsulated transition-metal nitrides as efficient Fenton-like catalysts, ACS Nano 10 (2016) 11532–11540, https://doi.org/10.1021/acsnano.6b07522.
[31] D.C. Marcano, D.V. Kosynkin, J.M. Berlin, A. Sinitskii, Z. Sun, A. Slesarev, L. B. Alemany, W. Lu, J.M. Tour, Improved synthesis of graphene oxide, ACS Nano 4 (2010) 4806–4814, https://doi.org/10.1021/nn1006368.
[32] P. Li, H.C. Zeng, Sandwich-Like Nanocomposite of CoNiOₓ/reduced graphene oxide for enhanced electrocatalytic water oxidation, Adv. Funct. Mater. 27 (2017) 10, https://doi.org/10.1002/adfm.201606325.
[33] P. Li, R. Chen, Y. Lin, W. Li, General approach to construct hierarchical-structured porous Co–Ni bimetallic oxides for efficient oxygen evolution, Inorg. Chem. Front. 7 (2020) 2611–2620, https://doi.org/10.1039/D0QI00463D.
[34] P. Li, H.C. Zeng, Hierarchical nanocomposite by the integration of reduced graphene oxide and amorphous carbon with ultrafine MgO nanocrystallites for enhanced CO₂ capture, Environ. Sci. Technol. 51 (2017) 12998–13007, https://doi.org/10.1021/acs.est.7b03308.
[35] P. Li, R. Chen, Y. Lin, W. Li, General approach to facile synthesis of MgO-based porous ultrathin nanosheets enabling high-efficiency CO₂ capture, Chem. Eng. J. 404 (2021), 126459, https://doi.org/10.1016/j.cej.2020.126459.
[36] L.L. Wang, X. Guo, Y.Y. Chen, S.S. Ai, H.M. Ding, Cobalt-doped g-C₃N₄ as a heterogeneous catalyst for photo-assisted activation of peroxymonosulfate for the degradation of organic contaminants, Appl. Surf. Sci. 467 (2019) 954–962, https://doi.org/10.1016/j.apsusc.2018.10.262.
[37] P.Z. Chen, K. Xu, Y. Tong, X.L. Li, S. Tao, Z.W. Fang, W.S. Chu, X.J. Wu, C.Z. Wu, Cobalt nitrides as a class of metallic electrocatalysts for the oxygen evolution reaction, Inorg. Chem. Front. 3 (2016) 236–242, https://doi.org/10.1039/c5qi00197h.
[38] S.H. Cho, K.R. Yoon, K. Shin, J.W. Jung, C. Kim, J.Y. Cheong, D.Y. Youn, S. W. Song, G. Henkelman, I.D. Kim, Synergistic coupling of metallic cobalt nitride nanofibers and irox nanoparticle catalysts for stable oxygen evolution, Chem. Mater. 30 (2018) 5941–5950, https://doi.org/10.1021/acs.chemmater.8b02061.
[39] N. Yao, P. Li, Z.R. Zhou, Y.M. Zhao, G.Z. Cheng, S.L. Chen, W. Luo, Synergistically tuning water and hydrogen binding abilities over Co₄N by Cr doping for exceptional alkaline hydrogen evolution electrocatalysis, Adv. Energy Mater. 9 (2019) 800, https://doi.org/10.1002/aenm.201902449.
[40] Q.C. Xu, H. Jiang, Y.H. Li, D. Liang, Y.J. Hu, C.Z. Li, In-situ enriching active sites on co-doped Fe-Co₄N@N-C nanosheet array as air cathode for flexible rechargeable

Zn-air batteries, Appl. Catal. B 256 (2019), 117893, https://doi.org/10.1016/j.apcatb.2019.117893.

[41] E. Saputra, S. Muhammad, H.Q. Sun, H.M. Ang, M.O. Tade, S.B. Wang, A comparative study of spinel structured Mn_3O_4, Co_3O_4 and Fe_3O_4 nanoparticles in catalytic oxidation of phenolic contaminants in aqueous solutions, J. Colloid Interface Sci. 407 (2013) 467–473, https://doi.org/10.1016/j.jcis.2013.06.061.

[42] L. Chen, Y. Huang, M. Zhou, K. Xing, L. Rao, W. Lv, Y. Yao, Enhanced peroxymonosulfate activation process based on homogenously dispersed iron and nitrogen active sites on a three-dimensional porous carbon framework, Chem. Eng. J. 404 (2021), 126537, https://doi.org/10.1016/j.cej.2020.126537.

[43] H. Li, C. Shan, W. Li, B. Pan, Peroxymonosulfate activation by iron(III)-tetraamidomacrocyclic ligand for degradation of organic pollutants via high-valent iron-oxo complex, Water Res. 147 (2018) 233–241, https://doi.org/10.1016/j.watres.2018.10.015.

[44] P. Fernández-Castro, M. Vallejo, M.F. San Román, I. Ortiz, Insight on the fundamentals of advanced oxidation processes. Role and review of the determination methods of reactive oxygen species, J. Chem. Technol. Biotechnol. 90 (2015) 796–820, https://doi.org/10.1002/jctb.4634.

[45] J.L. Wang, S.Z. Wang, Reactive species in advanced oxidation processes: formation, identification and reaction mechanism, Chem. Eng. J. 401 (2020), 126158, https://doi.org/10.1016/j.cej.2020.126158.

[46] S.S. Yang, P.X. Wu, J.Q. Liu, M.Q. Chen, Z. Ahmed, N.W. Zhu, Efficient removal of bisphenol A by superoxide radical and singlet oxygen generated from peroxymonosulfate activated with Fe^0-montmorillonite, Chem. Eng. J. 350 (2018) 484–495, https://doi.org/10.1016/j.cej.2018.04.175.

[47] C.Q. Li, Y. Huang, X.B. Dong, Z.M. Sun, X.D. Duan, B.X. Ren, S.L. Zheng, D. D. Dionysiou, Highly efficient activation of peroxymonosulfate by natural negatively-charged kaolinite with abundant hydroxyl groups for the degradation of atrazine, Appl. Catal. B 247 (2019) 10–23, https://doi.org/10.1016/j.apcatb.2019.01.079.

[48] L.L. Jiang, Y. Zhang, M.H. Zhou, L. Liang, K.R. Li, Oxidation of Rhodamine B by persulfate activated with porous carbon aerogel through a non-radical mechanism, J. Hazard. Mater. 358 (2018) 53–61, https://doi.org/10.1016/j.jhazmat.2018.06.048.

[49] M.A.N. Khan, P.K. Klu, C.H. Wang, W.X. Zhang, R. Luo, M. Zhang, J.W. Qi, X. Y. Sun, L.J. Wang, J.S. Li, Metal-organic framework-derived hollow Co_3O_4/carbon as efficient catalyst for peroxymonosulfate activation, Chem. Eng. J. 363 (2019) 234–246, https://doi.org/10.1016/j.cej.2019.01.129.

[50] F.L. Wang, Y.F. Wang, Y.L. Wu, D.D. Wei, L. Li, Q.X. Zhang, H.J. Liu, Y. Liu, W. Y. Lv, G.G. Liu, Template-free synthesis of oxygen-containing ultrathin porous carbon quantum dots/g-C_3N_4 with superior photocatalytic activity for PPCPs remediation, Environ. Sci. Nano 6 (2019) 2565–2576, https://doi.org/10.1039/c9en00509a.

[51] M. Zhu, J. Miao, X.G. Duan, D.Q. Guan, Y.J. Zhong, S.B. Wang, W. Zhou, Z.P. Shao, Postsynthesis growth of CoOOH nanostructure on $SrCo_{0.6}Ti_{0.4}O_{3-\delta}$ perovskite surface for enhanced degradation of aqueous organic contaminants, ACS Sustain. Chem. Eng. 6 (2018) 15737–15748, https://doi.org/10.1021/acssuschemeng.8b04289.

[52] Y.K. Long, Y.X. Huang, H.Y. Wu, X.W. Shi, L. Xiao, Peroxymonosulfate activation for pollutants degradation by Fe-N-codoped carbonaceous catalyst: Structure-dependent performance and mechanism insight, Chem. Eng. J. 369 (2019) 542–552, https://doi.org/10.1016/j.cej.2019.03.097.

[53] P. Liang, C. Zhang, X.G. Duan, H.Q. Sun, S.M. Liu, M.O. Tade, S.B. Wang, An insight into metal organic framework derived N-doped graphene for the oxidative degradation of persistent contaminants: formation mechanism and generation of singlet oxygen from peroxymonosulfate, Environ. Sci. Nano 4 (2017) 315–324, https://doi.org/10.1039/c6en00633g.

[54] P. Li, H.C. Zeng, Advanced oxygen evolution catalysis by bimetallic Ni-Fe phosphide nanoparticles encapsulated in nitrogen, phosphorus, and sulphur tri-doped porous carbon, Chem. Commun. 53 (2017) 6025–6028, https://doi.org/10.1039/C7CC03005C.

[55] Y.P. Li, J.H. Zhang, Y. Liu, Q.Z. Qian, Z.Y. Li, Y. Zhu, G.Q. Zhang, Partially exposed RuP_2 surface in hybrid structure endows its bifunctionality for hydrazine oxidation and hydrogen evolution catalysis, Sci. Adv. 6 (2020), https://doi.org/10.1126/sciadv.abb4197.

[56] J. Lim, Y. Yang, M.R. Hoffmann, Activation of peroxymonosulfate by oxygen vacancies-enriched cobalt-doped black TiO_2 nanotubes for the removal of organic pollutants, Environ. Sci. Technol. 53 (2019) 6972–6980, https://doi.org/10.1021/acs.est.9b01449.

[57] X.B. Dong, X.D. Duan, Z.M. Sun, X.W. Zhang, C.Q. Li, S.S. Yang, B.X. Ren, S. L. Zheng, D.D. Dionysiou, Natural illite-based ultrafine cobalt oxide with abundant oxygen-vacancies for highly efficient Fenton-like catalysis, Appl. Catal. B 261 (2020) 15, https://doi.org/10.1016/j.apcatb.2019.118214.

[58] X. Li, X. Huang, S. Xi, S. Miao, J. Ding, W. Cai, S. Liu, X. Yang, H. Yang, J. Gao, J. Wang, Y. Huang, T. Zhang, B. Liu, Single cobalt atoms anchored on porous n-doped graphene with dual reaction sites for efficient Fenton-like catalysis, J. Am. Chem. Soc. 140 (2018) 12469–12475, https://doi.org/10.1021/jacs.8b05992.

[59] A.J. Medford, A. Vojvodic, J.S. Hummelshøj, J. Voss, F. Abild-Pedersen, F. Studt, T. Bligaard, A. Nilsson, J.K. Nørskov, From the Sabatier principle to a predictive theory of transition-metal heterogeneous catalysis, J. Catal. 328 (2015) 36–42, https://doi.org/10.1016/j.jcat.2014.12.033.

[60] C. Wei, Y. Sun, G.G. Scherer, A.C. Fisher, M. Sherburne, J.W. Ager, Z.J. Xu, Surface composition dependent ligand effect in tuning the activity of nickel–copper bimetallic electrocatalysts toward hydrogen evolution in alkaline, J. Am. Chem. Soc. 142 (2020) 7765–7775, https://doi.org/10.1021/jacs.9b12005.

[61] H.Q. Sun, S.Z. Liu, G.L. Zhou, H.M. Ang, M.O. Tade, S.B. Wang, Reduced graphene oxide for catalytic oxidation of aqueous organic pollutants, ACS Appl. Mater. Interfaces 4 (2012) 5466–5471, https://doi.org/10.1021/am301372d.

[62] X. Cheng, H.G. Guo, Y.L. Zhang, X. Wu, Y. Liu, Non-photochemical production of singlet oxygen via activation of persulfate by carbon nanotubes, Water Res. 113 (2017) 80–88, https://doi.org/10.1016/j.watres.2017.02.016.

[63] Y. Li, D.D. Li, S.S. Fan, T. Yang, Q. Zhou, Facile template synthesis of dumbbell-like Mn_2O_3 with oxygen vacancies for efficient degradation of organic pollutants by activating peroxymonosulfate, Catal. Sci. Technol. 10 (2020) 864–875, https://doi.org/10.1039/c9cy01849b.